Inorganic Chemistry

Article

pubs.acs.org/IC

Fabrication of Novel p-BiOI/n-$ZnTiO_3$ Heterojunction for Degradation of Rhodamine 6G under Visible Light Irradiation

K. Hemalata Reddy, Satyabadi Martha, and K.M. Parida*

Colloids and Materials Chemistry Department, CSIR-Network Institute for Solar Energy, CSIR-Institute of Minerals and Materials Technology, Bhubaneswar −751013, Orissa, India

ABSTRACT: With the purpose of efficient electron−hole separation and enhancement of photocatalytic performance in the visible region, we have fabricated a novel p-BiOI/n-$ZnTiO_3$ heterojunction by a precipitation−deposition method and studied its activity toward dye degradation. The physicochemical characteristics of the fabricated BiOI/$ZnTiO_3$ heterojunctions were surveyed by powder X-ray diffraction pattern (PXRD), BET-surface area, diffuse reflectance UV−vis (DRUV−vis), field emission scanning electron microscopy (FESEM), transmission electron microscopy (TEM), photoluminescence spectroscopy (PL spectra), X-ray photoelectron spectroscopy (XPS), and photoelectrochemical measurement. The photosensitization effect of BiOI enhanced the spectral response of $ZnTiO_3$ from UV to visible region, making all the BiOI/$ZnTiO_3$ heterojunctions active under visible light. The PEC measurement confirmed the p-type character of BiOI and n-type character of $ZnTiO_3$. The optimal amount of BiOI in BiOI/$ZnTiO_3$ heterojunctions was found to be 50% which degraded 82% of 50 ppm Rh 6G under visible light irradiation. The degradation rate of 50% BiOI/$ZnTiO_3$ heterojunction was found to be 9.8 and 11.1 times higher than that of bare BiOI and $ZnTiO_3$, respectively. The photosensitization effect of BiOI and the formed heterojunction between p-type BiOI and n-type $ZnTiO_3$ contribute to improved electron−hole separation and enhancement in photocatalytic activity.

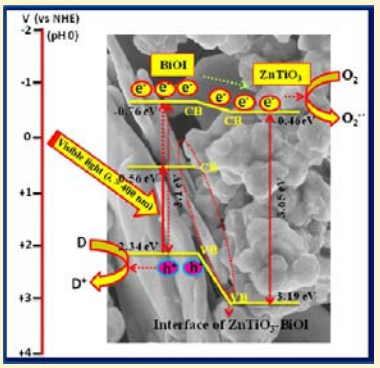

1. INTRODUCTION

Heterogeneous photocatalysis has become one of the most promising "green" technologies to triumph over the global energy demand and environment related dilemma.[1] Over a few decades, it has been reported that oxide based semiconductors are active photocatalysts in solar energy conversion for water decontamination and water splitting reaction.[2,3] However, most of the active oxides are perovskite-based mixed metal oxides with general formula ABO_3.[4−6] Particularly, the titanium based perovskite-type oxides, i.e., $MTiO_3$ (M= Sr, Ba, Pb, and Zn), are well-known semiconductors which are used for water splitting and dye degradation reactions.[6−9] Among them, $ZnTiO_3$ is an attractive runner in the application fields of gas sensor, microwave dielectrics, white pigment, photocatalysis, and catalytic sorbents for desulfurization of hot coal.[9−13] Especially, the cubic $ZnTiO_3$ has potential applications in various fields such as nonlinear optics, photocatalysis, antibacterial properties, and photoluminescence studies.[14,15] For photocatalytic application, the development of visible light responsive materials is necessary for proper utilization of solar light because it occupies 43% of the solar spectrum. However, the wide band gap of cubic $ZnTiO_3$ (3.65 eV) limits its activity to the UV region. Therefore, our aim is to shift the optical absorption of $ZnTiO_3$ from the UV to the visible spectral range and improve the photocatalytic activity. Currently, the coupling of two semiconductors is making headlines in the research area due to their promising properties like improvement of photoabsorption of the UV active materials in the visible region and also suppression of the recombination rate of the charge carriers.[16,17] Moreover, the coupling of two different semiconductors should have proper band edge potentials which help to transfer the charge carriers from one semiconductor to the other. This favors the separation of photoinduced electrons and holes and thus improves the photocatalytic efficiency of the materials.[18] Particularly, the coupling of p- and n-type semiconductors is believed to be helpful because an internal electric field is built up when a junction is formed between them.[19] Therefore, the coupling of n-type $ZnTiO_3$with p-type narrow band gap semiconductors is a good strategy to improve the visible light absorption capability and the photocatalytic performance of $ZnTiO_3$ under visible light irradiation. Most p-type narrow band gap semiconductors which have shown excellent photocatalytic activities under visible light irradiation are related to the bismuth-containing materials, such as Bi_2O_3 and BiOX (X = Br and I).[20−22]

Among them, BiOI is an attractive p-type semiconductor with strongest photoresponse in the visible light region due to its narrow band gap energy (1.78 eV) and is a potential sensitizer to sensitize wide band gap semiconductors.[23,24] By now, a number of BiOI-based heterojunctions, such as TiO_2/BiOI,[18,24,25] Bi_2S_3/BiOI,[26] ZnO/BiOI,[27] AgI/BiOI,[28] BiOI/Bi_2O_3,[29] Pt/BiOI,[30] BiOCl/BiOI,[31] $Bi_2O_2CO_3$/BiOI,[32] and Ag/BiOI,[33]have been reported for photocatalytic reaction, and their results show that BiOI-based heterojunctions exhibit enhanced photocatalytic performance under visible light irradiation. To

Received: January 21, 2013
Published: May 14, 2013

   dx.doi.org/10.1021/ic400159m | *Inorg. Chem.* 2013, 52, 6390−6401

the best of our knowledge, the coupling of p-type BiOI with n-type $ZnTiO_3$ for photocatalytic purpose has not been reported previously.

In this Article, we fabricate a series of p-BiOI/n-$ZnTiO_3$ heterojunctions by a precipitation−deposition method[22] and examine their photocalytic performance toward Rhodamine 6G degradation under visible light irradiation. Our results indicate that the p-type BiOI enhances the photoabsorption capability of $ZnTiO_3$ in the visible region. The formed p−n junction between BiOI and $ZnTiO_3$ improves the separation efficiency of the charge carriers which leads to the enhanced photocatalytic activity for Rhodamine 6G degradation. The kinetics and the possible photocatalytic mechanism of the p-BiOI/n-$ZnTiO_3$ heterojunction related to the band positions of the two semiconductors are discussed in detail.

2. MATERIALS AND METHODS

Synthesis of $ZnTiO_3$. $ZnTiO_3$ powder was prepared by a sol−gel method.[34,35]Analytical grade $Zn(CH_3COO)_2{\cdot}2H_2O$, $Ti(OC_4H_9)_4$, absolute ethanol (C_2H_5OH), ethylene glycol ($HOCH_2CH_2OH$), and HNO_3 were used as raw materials to prepare $ZnTiO_3$. Titanium butoxide was dissolved in absolute ethanol (purity of 99.5%) and vigorously stirred for 30 min. The obtained solution was then added dropwise to the solution containing ethanol, water, and a few drops of HNO_3 and again stirred for 2 h in order to obtain a homogeneous solution. The molar ratio of $Ti(OC_4H_9)_4/C_2H_5OH/H_2O$ was 1/25.4/1. The solution of zinc acetate ($Zn(CH_3COO)_2{\cdot}2H_2O$) prepared in ethylene glycol ($HOCH_2CH_2OH$) was then added slowly into the TiO_2 sol under stirring (Zn/Ti = 1/1). The mixture was stirred for 1 h, which led to the formation of a homogeneous gel. The obtained gel was dried at 110 °C for 5 h and activated at 600 °C for 2 h in air.

Synthesis of BiOI-$ZnTiO_3$ Heterojunctions. The BiOI−$ZnTiO_3$ heterojunctions were prepared by a precipitation−deposition method. A measured amount of $Bi(NO_3)_3{\cdot}5H_2O$ was dissolved in 100 mL of distilled water containing 10 mL of glacial acetic acid and stirred for 10 min to get a clear solution. Then, the prepared $ZnTiO_3$ was added into the clear solution. The mixture was vigorously stirred for 30 min at room temperature. The amount of $Bi(NO_3)_3{\cdot}5H_2O$ was varied to obtain BiOI/$ZnTiO_3$ heterojunctions with molar ratio of 0, 10%, 30%, 50%, 70%, and 90%, respectively. The resulting mixed solution was added rapidly to 30 mL of distilled water containing stoichiometric amounts of KI (AR, BDH, 99.0%). On adding, cream pink-deep red precipitate was immediately formed with the variation of $Bi(NO_3)_3{\cdot}5H_2O$ concentration from 10 to 90 mol %. The obtained precipitate was stirred for another 30 min at room temperature, and the suspension was aged for 3 h. The resulting precipitate was filtered, washed thoroughly with distilled water, and then dried at 65 °C for overnight.[22] The neat BiOI was prepared by the same method without using $ZnTiO_3$ precursor.

Photocatalytic Degradation of Rhodamine 6G. Photocatalytic degradation of Rhodamine 6G (50 mg/L) was carried out in a quartz reactor by taking 0.02 g of catalyst in 20 mL of synthetic aqueous Rhodamine 6G solution under visible light illumination ($\lambda \geq 400$ nm) for 180 min in an irradiation chamber (BS 02, Dr. Gröbel, UV-Elektronik GmbH). Prior to irradiation, dark adsorption experiments were carried out for 1 h under continuous stirring. After irradiation, the suspension was centrifuged, and then the residual concentration of Rhodamine 6G was estimated spectrophotometrically at 547 nm using a Varian Cary 100 UV−vis spectrophotometer.[36] Rhodamine 6G is named as Rh 6G afterward.

Methods of Characterization. The samples were characterized by powder X-ray diffraction pattern (PXRD), BET-surface area, diffuse reflectance UV−vis (DRUV−vis), field emission scanning electron microscopy (FESEM), transmission electron microscopy (TEM), high resolution transmission electron microscopy (HRTEM), energy dispersive X-ray spectroscopy (EDAX), photoluminescence spectroscopy (PL spectra), X-ray photoelectron spectroscopy (XPS), and photoelectrochemical measurement. The PXRD patterns were collected using a RINT-Ultima III, Rigaku diffractometer with automatic control. The patterns were run with monochromatic Cu Kα radiation with 2θ = 10−80° with a scan rate of 2°/min. FESEM images were taken on a Zeiss Supra 55. TEM and HRTEM were obtained on Philips TECNAI G^2 operated at 200 kV, in which the specimen was prepared by dispersing the powdered samples in 2-propanol, sonicating for 3 min, and then drop-drying on a copper grid coated with carbon film. PL spectra were recorded with a Perkin-Elmer (LS 55) spectrofluorimeter. The PL spectra were measured at room temperature under excitation at 350 nm provided by emission from a xenon lamp. Optical absorbance was measured by DRUV−vis spectra of the catalyst samples with a Varian Cary 100 spectrophotometer equipped with a diffuse reflectance accessory in the region 200−800 nm, with boric acid as the reference. XPS measurements were performed on a VG Microtech Multilab ESCA 3000 spectrometer with a nonmonochromatised Mg Kα X-ray source. The binding energy correction was performed using the C 1s peak of carbon at 284.9 eV as reference. For photoelectrochemical measurement, the electrodes were prepared by electrophoretic deposition in an acetone solution (30 mL) containing photocatalysts powder (30 mg) and iodine (30 mg). Two parallel FTO (fluorine doped tin oxide) electrodes were immersed in the solution with a 10−15 mm separation, and a 50 V bias was applied between the two for 3 min under potentiostat control. The coated area was fixed at either 1 cm × 3 cm and then dried. The photoelectrochemical measurement was performed using a conventional Pyrex electrochemical cell consisting of a prepared electrode, a platinum wire as a counter electrode (1 mm in diameter, 15 mm in length), and an Ag/AgCl reference electrode. The cell was filled with an aqueous solution of 0.1 M Na_2SO_4, and the pH of the solution was adjusted to 6. The electrolyte was saturated with nitrogen prior to electrochemical measurements, and the potential of the electrode was controlled by a potentiostat (Versastat 3, Princeton Applied Research) with 300 W Xe lamp. It should be noted that the FTO (fluorine doped tin oxide) did not show photoresponse in the solution. For $OH^{\bullet}$ radical detection, the experimental procedure is similar as that of the photocatalytic process, except that the aqueous solution of Rh 6G was replaced by a 5×10^{-4} M terephthalic acid (TA) solution with 2×10^{-3} M NaOH solution. The fluorescence spectra were measured on a FLUOROMAX-4p spectrophotometer. The reaction solution emits fluorescence spectra around 425 nm on excitation at 315 nm.[37]

3. RESULTS AND DISCUSSION

Structural Characterization. The structure identity and phase composition of pure $ZnTiO_3$, BiOI, and BiOI/$ZnTiO_3$ heterojunctions were confirmed by powder X-ray diffraction (PXRD) patterns. Figure 1 displays the powder X-ray diffraction (PXRD) patterns of BiOI/$ZnTiO_3$ heterojunctions with varying BiOI contents along with pure $ZnTiO_3$ and BiOI for comparison study. All the characteristic diffraction peaks in Figure 1a can be perfectly assigned as the cubic phase of $ZnTiO_3$ which coincides well with the standard data of $ZnTiO_3$ (JCPDS card 36-0190) whereas the diffraction patterns of pure BiOI are consistent with the tetragonal phase of BiOI (JCPDS card 40-0445) as shown in Figure 1g. The diffraction peaks of both BiOI and $ZnTiO_3$ became narrow and well-defined which reveals that the samples have high degree of crystallinity. The absence of any impurity related peaks in the diffraction patterns of BiOI and $ZnTiO_3$ samples confirmed the high purity of the two products. Structurally, the BiOI/$ZnTiO_3$ heterojunctions present a two-phase composition, i.e., tetragonal phase of BiOI and the cubic phase of $ZnTiO_3$ with no other impurity peaks from the diffraction patterns. Therefore, the BiOI/$ZnTiO_3$ heterojunctions contained only $ZnTiO_3$ and BiOI components. The intense peak of all the BiOI/$ZnTiO_3$ heterojunctions indicates that the samples are well crystallized. The tetragonal BiOI diffraction peaks began to appear and are gradually intensified with an increasing amount of BiOI from 10% to 90%

dx.doi.org/10.1021/ic400159m | Inorg. Chem. 2013, 52, 6390−6401

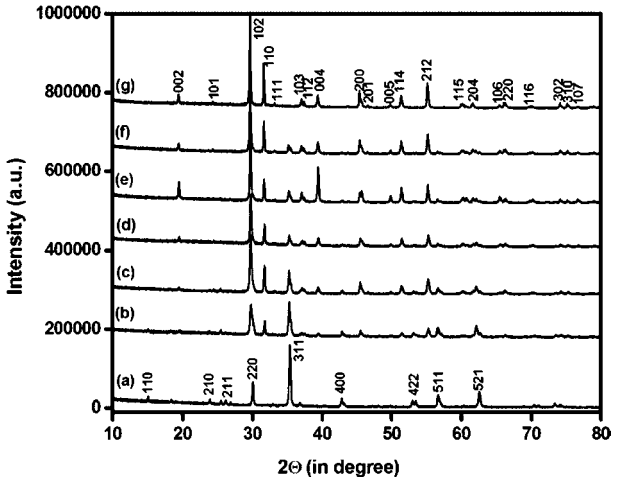

Figure 1. X-ray diffraction patterns of (a) $ZnTiO_3$, (b) 10 mol % $BiOI/ZnTiO_3$, (c) 30 mol % $BiOI/ZnTiO_3$, (d) 50 mol % $BiOI/ZnTiO_3$, (e) 70 mol % $BiOI/ZnTiO_3$, (f) 90 mol % $BiOI/ZnTiO_3$, (g) BiOI.

in the $BiOI/ZnTiO_3$ heterojunction powders as shown in Figure 1b–f.

The diffraction peak intensity ratio of $I_{BiOI(102)}/I_{ZnTiO3(311)}$ between the two components gradually increases with increasing BiOI molar ratio in the $BiOI/ZnTiO_3$ heterojunctions and vice versa as shown in Figure 2a. Furthermore, the diffraction peaks assigned to $ZnTiO_3$ in the patterns of $BiOI/ZnTiO_3$ heterojunctions became weaker, which suggests that the presence of BiOI could inhibit the crystal growth of $ZnTiO_3$.[18,27] The main diffraction peaks of $ZnTiO_3$ (311) in $BiOI/ZnTiO_3$ heterojunctions were slightly shifted to lower angle region compared to neat $ZnTiO_3$, and the diffraction peaks of BiOI (102) were slightly shifted to higher angle region in comparison to their neat BiOI samples as shown in Figure 2b,c. This indicates that the interaction takes place between $ZnTiO_3$ and BiOI crystals in the heterojunctions.

The average crystallite size of the fabricated samples were estimated by using Scherrer eq 1:

$$D = k\lambda/\beta\cos\theta \quad (1)$$

Here, D is the crystallite size, k is a correction factor, which is taken as 0.9, β is the full width at half-maximum (fwhm) of the most intense diffraction peak of 311 plane of $ZnTiO_3$ and 102 plane of BiOI, respectively, λ is the wavelength of the Cu target (1.5406 Å), and θ is the Bragg diffraction angle. The average crystallite size of the pure BiOI and $ZnTiO_3$ was found to be 51.16 and 45.53 nm, respectively. However, in the case of $BiOI/ZnTiO_3$ heterojunctions, the crystallite size of $ZnTiO_3$ decreases with increasing BiOI amount while the crystallite size

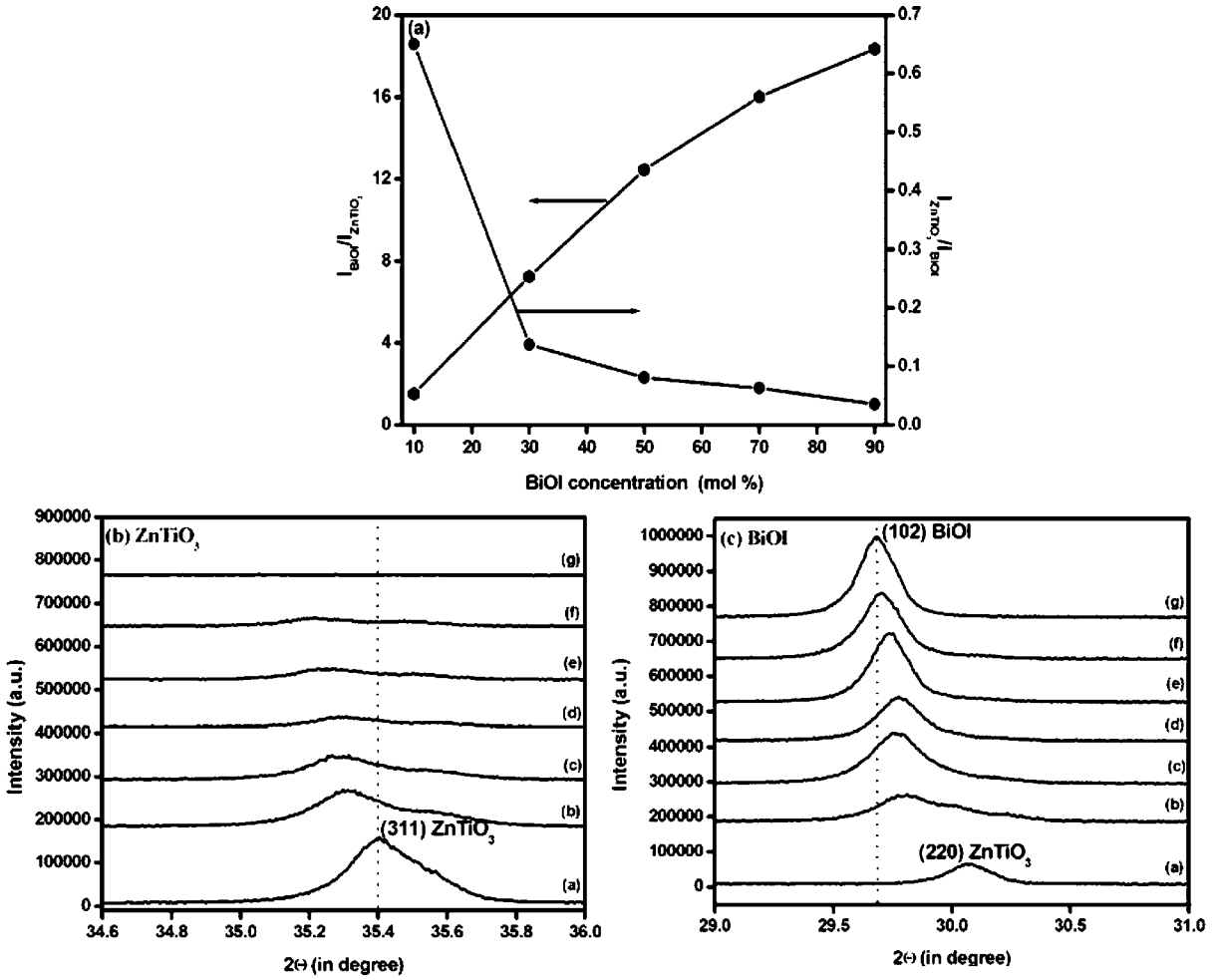

Figure 2. (a) Diffraction peak intensity ratio of $I_{BiOI(102)}/I_{ZnTiO3(311)}$ and $I_{ZnTiO3(311)}/I_{BiOI(102)}$, and enlarged profile of the (311) diffraction pattern of $ZnTiO_3$ as shown in part b and (102) diffraction pattern of BiOI as shown in part c.

dx.doi.org/10.1021/ic400159m | Inorg. Chem. 2013, 52, 6390–6401

of BiOI increases as shown in Table 1. This indicates that BiOI concentration strongly affects the size and growth of the $ZnTiO_3$ in the heterojunctions.

Table 1. Textural Properties of $ZnTiO_3$, BiOI, and BiOI/$ZnTiO_3$ Heterojunctions

	crystalite size (nm)			
catalyst	BiOI	$ZnTiO_3$	% of degradation	rate constant (s^{-1})
$ZnTiO_3$		45.53	15	0.0009
10 mol % BiOI/$ZnTiO_3$	32.7	40.15	38	0.0027
30 mol % BiOI/$ZnTiO_3$	34.53	38.2	50	0.0039
50 mol % BiOI/$ZnTiO_3$	42.58	36.5	82	0.0101
70 mol % BiOI/$ZnTiO_3$	45.14	35.6	70	0.0065
90 mol % BiOI/$ZnTiO_3$	49.21	35.1	54	0.0043
BiOI	51.16		18	0.0011

Morphological Characterization. The detailed morphology and microstructure of the pure $ZnTiO_3$, BiOI, and BiOI/$ZnTiO_3$ heterojunctions with different BiOI concentrations were inspected by FESEM and TEM. Figure 3 presents the surface view of FESEM images of the pure $ZnTiO_3$, BiOI, and BiOI/$ZnTiO_3$ heterojunctions with varying BiOI concentrations from 10 to 90 mol %. The morphology of the pure $ZnTiO_3$ appears to be irregular aggregates with size ranging between 100 and 500 nm (Figure 3a). The pure BiOI consists of a large quantity of irregular plates with smooth surface which are in the range of nanometer to micrometer in size. The close-up view of the large single BiOI plate in the Figure 3g indicates that it is built by the fusion of a huge number of nanoplates. In other words, the large irregular BiOI plates are composed of plenty of smooth nanoplates. The morphology of the BiOI/$ZnTiO_3$ heterojunctions with variation of BiOI concentration from 10 to 90 mol % is shown in Figure 3b–f. At lower concentration of BiOI (10–30 mol %), there is slight formation of BiOI plates along with $ZnTiO_3$ aggregates. This indicates that the BiOI nanoplates begin to grow which is specified by the arrow marks in the Figure 3b,c. The platelike morphology becomes prominent, and the size of the plates increases when the BiOI concentration is introduced more than 30 mol % in the BiOI/$ZnTiO_3$ heterojunctions. The intergrowth of BiOI nanoplates takes place as its concentration increases in the heterojunctions. The BiOI plates almost cover the $ZnTiO_3$ aggregates when its mole fraction reaches 90 mol %, and this may be the main reason for inhibition of the growth of $ZnTiO_3$ particles in the heterojunctions. Therefore, we conclude that morphologies of all the heterojunctions exhibit the coexistence of BiOI and $ZnTiO_3$. No other morphologies are observed in the FESEM images which indicate the purity of the products. The contact between $ZnTiO_3$ nanoparticles and BiOI plates is observed to be good at all the heterojunctions, facilitating the interparticle electron transfer between BiOI and $ZnTiO_3$.[38]

The interior structure of the pure $ZnTiO_3$, BiOI, and 50% BiOI/$ZnTiO_3$ heterojunctions was further analyzed by TEM. Figure 4a represents the typical TEM micrograph of $ZnTiO_3$,

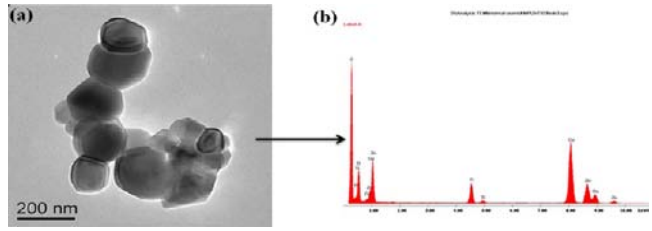

Figure 4. (a, b) TEM image and EDAX pattern of $ZnTiO_3$.

from which it is observed that $ZnTiO_3$ contains irregular particles with size ranging between 200 and 300 nm and is

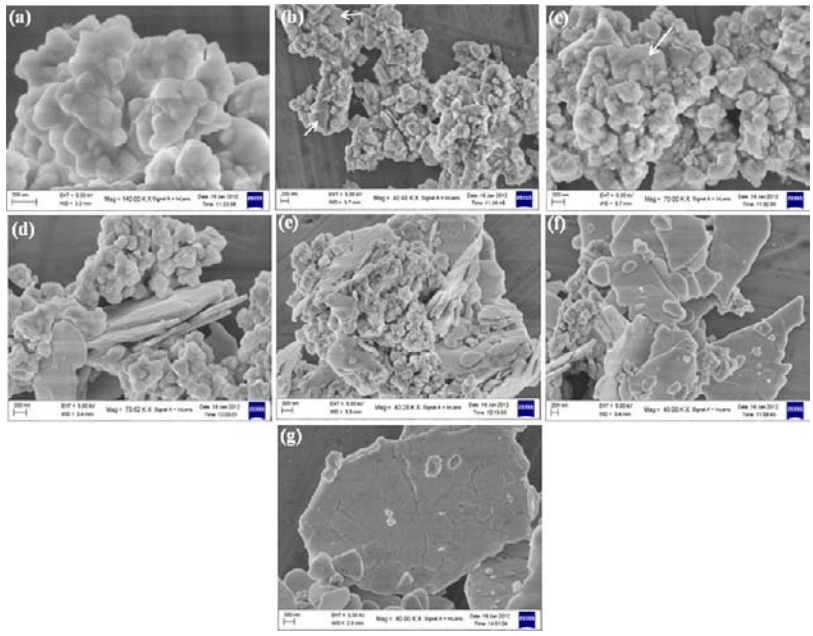

Figure 3. FESEM images of (a) $ZnTiO_3$, (b) 10 mol % BiOI/$ZnTiO_3$, (c) 30 mol % BiOI/$ZnTiO_3$, (d) 50 mol % BiOI/$ZnTiO_3$, (e) 70 mol % BiOI/$ZnTiO_3$, (f) 90 mol % BiOI/$ZnTiO_3$, (g) BiOI.

dx.doi.org/10.1021/ic400159m | Inorg. Chem. 2013, 52, 6390–6401

identical with the FESEM image. Figure 4b provides a representative EDAX pattern of $ZnTiO_3$ which shows the presence of Zn, Ti, and O elements in the sample. Figure 5a shows typical TEM image of the representative BiOI with plate-shape morphology whose size ranging from nanometer to micrometer scale is consistent with the FESEM observations. Figure 5b provides a representative EDAX pattern of a BiOI plate which shows the presence of Bi, O, and I elements in the sample. The selected area electron diffraction (SAED) pattern was taken by focusing the electron beam on a single BiOI plate (Figure 5c). The bright spots without concentric rings in the selected area electron diffraction (SAED) pattern illustrate the single crystalline nature of BiOI. The spots are related to the (102) and (200) planes indexed to tetragonal phase of single crystalline BiOI which is consistent with the XRD pattern.[39]

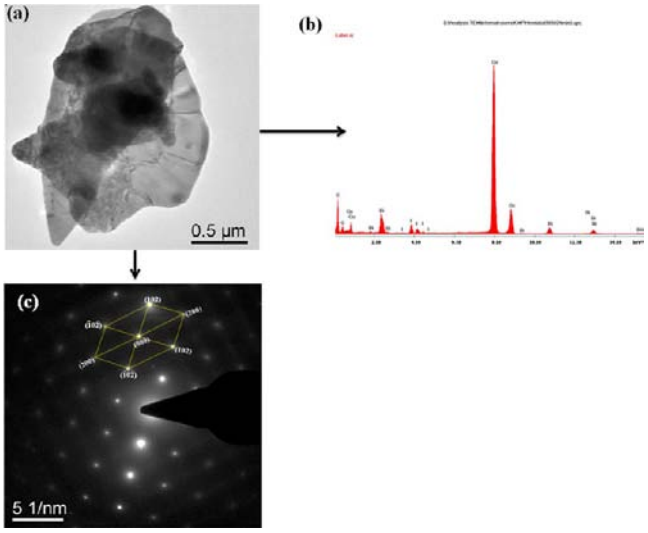

Figure 5. (a) TEM image, (b) EDAX, and (c) SAED pattern of BiOI.

The typical TEM image of the 50% $BiOI/ZnTiO_3$ heterojunction is shown in Figure 6a. The TEM micrograph shows that the $ZnTiO_3$ particles are deposited on the surface of the BiOI plates and the image is darker in comparison to that of neat BiOI plates (Figure 5a). The EDAX shows the presence of Zn, Ti, Bi, I, and O elements in the $BiOI/ZnTiO_3$ heterojunction as shown in Figure 6b. The selected area electron diffraction (SAED) patterns of the $BiOI/ZnTiO_3$ heterojunction are represented in Figure 6c. The SAED pattern of the $BiOI/ZnTiO_3$ heterojunction shows the coexistence of the tetragonal phase of BiOI and the cubic phase of $ZnTiO_3$ which coincides well with the XRD pattern. The brighter inner ring corresponds to the (311) plane of the cubic phase of $ZnTiO_3$, and the light spots correspond to the (102) and (200) planes of the tetragonal phase of BiOI. The bright ring pattern shows the polycrystalline nature of $ZnTiO_3$, and the bright spots without rings confirm the single crystalline nature of BiOI. The SAED pattern of the $BiOI/ZnTiO_3$ heterojunction confirms that the product is well crystallized. The discontinuous state in the ring pattern of $ZnTiO_3$ in the $BiOI/ZnTiO_3$ heterojunction may arise due to some disturbance in the arrangement of the $ZnTiO_3$ particles in three-dimensional space, and this disturbance is attributed to coupling of $ZnTiO_3$ with BiOI with their heterotype morphology.[39] The bright and dark-field images are again taken to confirm the presence of $ZnTiO_3$ particles on the surface of BiOI plates as shown in Figure 7a,b. The glowing particles in the image in part b are ascribed to the $ZnTiO_3$ particles, and the dark portion is assigned to the BiOI plate. The bright and dark images of a

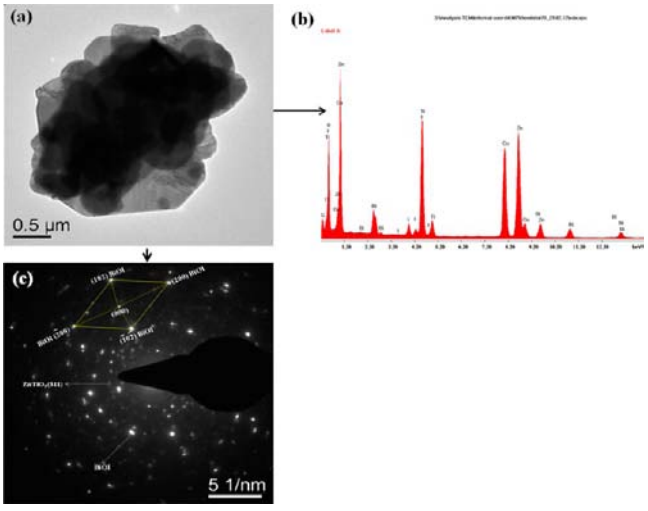

Figure 6. (a) TEM image, (b) EDAX, and (c) SAED pattern of 50% $BiOI/ZnTiO_3$ heterojunction.

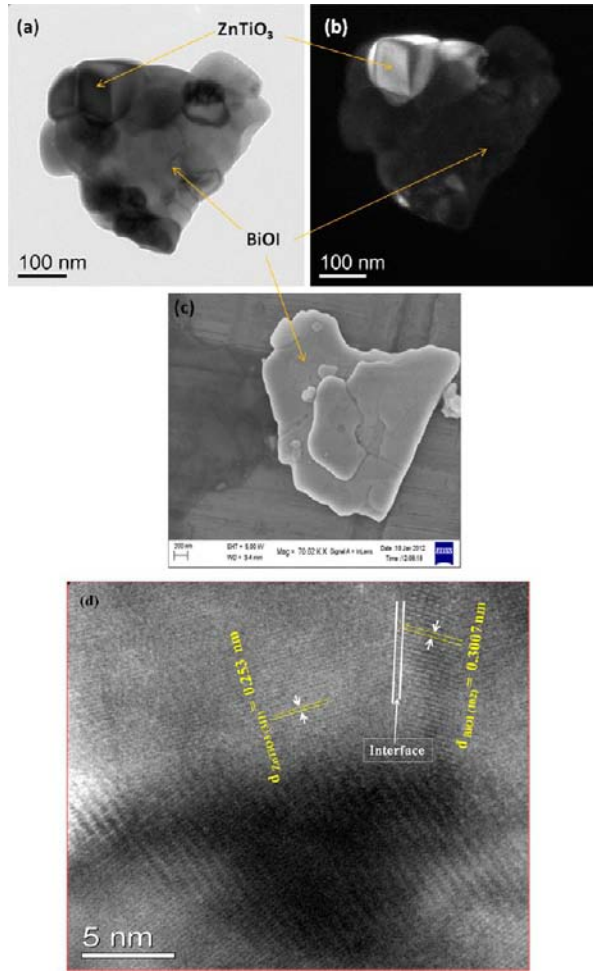

Figure 7. (a and b) Bright and dark field images of 50% $BiOI/ZnTiO_3$ heterojunction and (c) FESEM image of neat BiOI plate. (d) HRTEM image of 50% $BiOI/ZnTiO_3$ heterojunction.

dx.doi.org/10.1021/ic400159m | Inorg. Chem. 2013, 52, 6390−6401

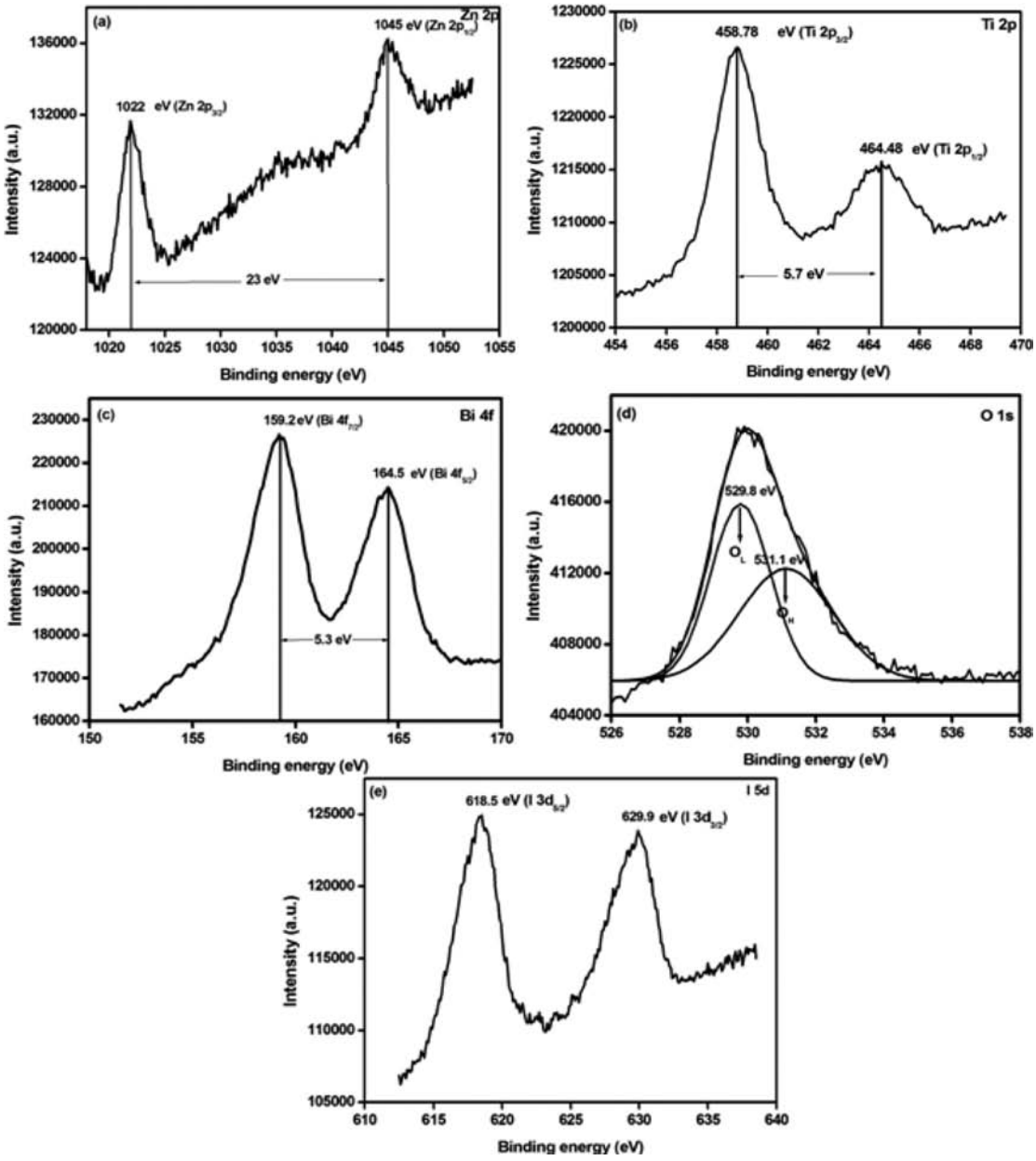

Figure 8. XPS spectra for BiOI/$ZnTiO_3$ in the regions of (a) Zn 2p, (b) Ti 2p, (c) Bi 4f, (d) O 1s, and (e) I 5d.

BiOI/$ZnTiO_3$ heterojunction show the tight contact between $ZnTiO_3$ particles and BiOI plates, which is again confirmed by the HRTEM. The plate structure of BiOI obtained in the bright and dark images of BiOI/$ZnTiO_3$ heterojunction is well matched with the FESEM image as shown in Figure 7c. Therefore, the bright and dark field images confirm the presence of two types of crystals in the BiOI/$ZnTiO_3$ heterojunction. The HRTEM image of the BiOI/$ZnTiO_3$ heterojunction is shown in Figure 7d. The observed lattice spacings of 0.301 and 0.253 nm correspond to the (102) and (311) planes of the tetragonal BiOI and cubic $ZnTiO_3$. The HRTEM image reveals the highly crystalline nature of BiOI/$ZnTiO_3$.The good crystallinity and the clear interface between $ZnTiO_3$ and BiOI are advantageous for the separation of the photogenerated charge carriers.[40]

X-ray Photoelectron Spectroscopy. The chemical state and surface composition of the 50% BiOI/$ZnTiO_3$ heterojunction were studied by X-ray photoemission spectroscopy (XPS). Figure 8 represents the high resolution XPS spectra of the Zn 2p, Ti 2p, Bi 4f, O 1s, and I 5d peaks of the 50% BiOI/$ZnTiO_3$ heterojunction which indicates that all the elements exist in the 50% BiOI/$ZnTiO_3$ heterojunction. Figure 8a represents the two individual symmetric peaks for the Zn 2p region. The peak positioned at 1022 eV was ascribed to the Zn $2p_{3/2}$ state, and another one positioned at 1045 eV was assigned to Zn $2p_{1/2}$. The peak separation between the Zn $2p_{3/2}$ and Zn $2p_{1/2}$ is 23 eV, assigned to the +2 oxidation state of zinc in BiOI/$ZnTiO_3$ heterojunction.[41,42] As shown in Figure 8b, there are two symmetric peaks in the Ti 2p region. The two symmetric peaks of Ti 2p located at 458.78 and 464.48 eV were ascribed to the Ti $2p_{3/2}$ and Ti $2p_{1/2}$, respectively. The peak separation between the Ti $2p_{3/2}$ and Ti $2p_{1/2}$ is 5.7 eV, which indicates a +4 oxidation state of Ti in the BiOI/$ZnTiO_3$ heterojunctions.[43]The binding energy values of both Zn 2p and Ti 2p are shifted toward higher binding energy values in comparison to the reported values of pure ZnO and TiO_2.

dx.doi.org/10.1021/ic400159m | Inorg. Chem. 2013, 52, 6390−6401

However, their peak separation values remain the same as that of the corresponding pure compounds. Therefore, we conclude that the shifting of Zn 2p and Ti 2p peaks toward higher binding energy region with fixed peak difference indicates the interatomic interactions in the (Ti−O−Zn) linkage of cubic $ZnTiO_3$ in the $BiOI/ZnTiO_3$ heterojunction.[41,42] The two strong peaks at 159.2 and 164.5 eV are assigned to Bi $4f_{5/2}$ and Bi $4f_{7/2}$ peaks of Bi^{3+} in the $BiOI/ZnTiO_3$ heterojunction with a peak difference of 5.3 eV as shown in Figure 8c.[44] On the other hand, the O 1s peak was deconvoluted into two individual peaks. The lower binding energy peak position at 529.8 eV was attributed to the lattice oxygen. The lattice oxygen peak is related to the Ti−O, Zn−O, and Bi−O chemical bonding in the $BiOI/ZnTiO_3$ heterojunction.[45]The higher binding energy peak positioned at 531.1 eV was attributed to the surface hydroxyl oxygen as shown in Figure 8d. The XPS spectra of I 3d is shown in Figure 8e. The binding energies of I $3d_{5/2}$ and I $3d_{3/2}$ located at 618.5 and 629.9 eV, respectively, were assigned to the −1 oxidation state of iodine.[32]

BET Surface Area. The BET surface areas of $ZnTiO_3$, BiOI, and 50% $BiOI/ZnTiO_3$ heterojunction are 2.6, 3.5, and 7.8 m^2g^{-1}, respectively. The heterojunction has a higher BET surface area than that of pure $ZnTiO_3$ and BiOI. The increase in BET surface area may be due to the crystal growth inhibition effect between the two components.[27]

Optical Absorption Properties. The light absorption properties of the neat $ZnTiO_3$, BiOI, and $BiOI/ZnTiO_3$ heterojunctions were characterized by UV−vis diffuse reflectance spectroscopy. Figure 9 shows the effect of BiOI concentration on the optical properties of $ZnTiO_3$. The optical absorption edges of the pure $ZnTiO_3$ and BiOI were roughly estimated from the absorption onset located at about 340 and 696 nm, respectively. The observed result indicates that the pure $ZnTiO_3$ had no significant absorption in the visible region whereas the BiOI had broad absorption in the visible region. When $ZnTiO_3$ combines with different concentrations of BiOI, the optical response of all the combined samples appears in the visible region. This is due to the superposition of the absorption of the two components. Moreover, the color of the $BiOI/ZnTiO_3$ heterojunctions changes from cream pink to orange red with increasing BiOI concentration from 10 to 90 mol % whereas pure $ZnTiO_3$ is white in color and BiOI is deep red in color. The visible light absorption of $BiOI/ZnTiO_3$ was only due to the contribution of BiOI, since $ZnTiO_3$ had no absorption in the visible region. Furthermore, BiOI is a potential photosensitizer which sensitizes the wide band gap $ZnTiO_3$ semiconductor in the visible section. The BiOI with narrow band gap (1.78 eV) could be easily activated by visible light and induce photoelectrons and holes. In the absence of $ZnTiO_3$, these electrons and holes might recombine rapidly owing to the narrow band gap, leading to the quenching of spectral response. In $BiOI/ZnTiO_3$ heterojunctions, the photoelectrons could easily transfer from the conduction band (CB) of BiOI to the neighboring CB of $ZnTiO_3$. Thus, the recombination between photoelectrons and holes could be effectively inhibited, leading to the strong response in visible region.[45,46] The steep shape of the spectrum indicated that the visible light absorption was due to the band gap transition. The band gap energy of a semiconductor could be calculated by the following equation.[26]

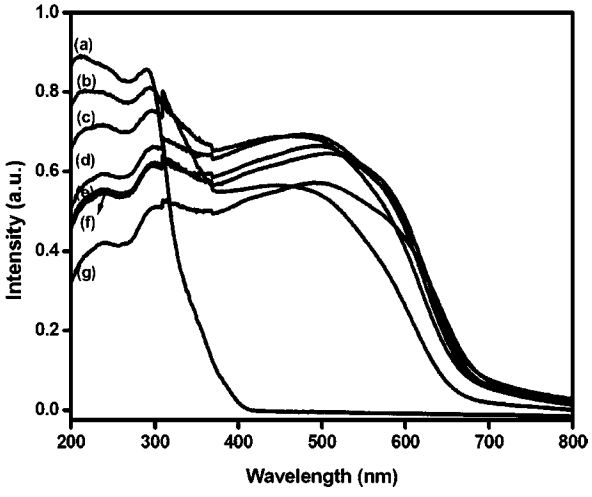

Figure 9. Photoabsorbance spectra of (a) $ZnTiO_3$, (b) 10 mol % $BiOI/ZnTiO_3$, (c) 30 mol % $BiOI/ZnTiO_3$, (d) 50 mol % $BiOI/ZnTiO_3$, (e) 70 mol % $BiOI/ZnTiO_3$, (f) 90 mol % $BiOI/ZnTiO_3$, (g) BiOI.

$$\alpha h\nu = A(h\nu - \mathrm{Eg})^{n/2} \quad (2)$$

Here, α, ν, Eg, and A are the absorption coefficient, light frequency, band gap energy, and a proportionality constant, respectively. Among them, n decides the kind of optical transition in a semiconductor (i.e., $n = 1$ for direct transition or $n = 4$ for indirect transition). The calculated n value for $ZnTiO_3$ is 1 and that for the BiOI is 4. This means that the optical transitions for the $ZnTiO_3$ are directly allowed and that for BiOI is indirectly allowed. The band gap energies of the $ZnTiO_3$ and BiOI samples can be estimated from the plots of $(\alpha h\nu)^2$ versus photon energy $(h\nu)$ and $(\alpha h\nu)^{1/2}$ versus photon energy $(h\nu)$, respectively. The intercept of the tangent to the X-axis would give a good approximation of the band gap energies for the synthesized products, as shown in Figure 10a,b. The estimated band gap energies of the resulting samples were about 3.65 and 1.78 eV for $ZnTiO_3$ and BiOI, respectively.

PL Spectroscopy. PL spectra originate from the migration, transfer, and separation efficiency of the photogenerated charge carriers in a semiconducting material.[47] There is a strong correlation between PL intensity and the photocatalytic performances. Higher PL intensity indicates the higher recombination of the charge carriers, which results in lower photocatalytic activity.[48] The comparison of PL spectra of $ZnTiO_3$ and 50% $BiOI/ZnTiO_3$ for excitation wavelength 350 nm is shown in Figure 11. The PL spectrum of the pure $ZnTiO_3$ shows an emission peak centered at 482 nm. This emission was not due to the band to band transition because the peak centered at 482 nm having 2.55 eV is much smaller than the optical band gap of the crystalline $ZnTiO_3$, i.e., 3.65 eV. Therefore, the emission might result from the defects existing in the $ZnTiO_3$ crystal.[14,49] The PL emission intensity of $BiOI/ZnTiO_3$ heterojunctions is relatively lower compared to that of pure $ZnTiO_3$. This is attributed to the fact that interfacial photogenerated electrons transfer from BiOI to $ZnTiO_3$ retards the charge recombination process.[48]

Photoelectrochemical Measurement. The semiconducting nature and the virtual band edge positions of $ZnTiO_3$ and BiOI semiconductors were determined by photoelectrochemical method. In heterojunction based materials, the direction of flow of charge carriers depends on their relative band edge positions. The photocurrent spectra of BiOI and $ZnTiO_3$ are shown in Figure 12a,b. From photocurrent spectra, it is

dx.doi.org/10.1021/ic400159m | Inorg. Chem. 2013, 52, 6390−6401

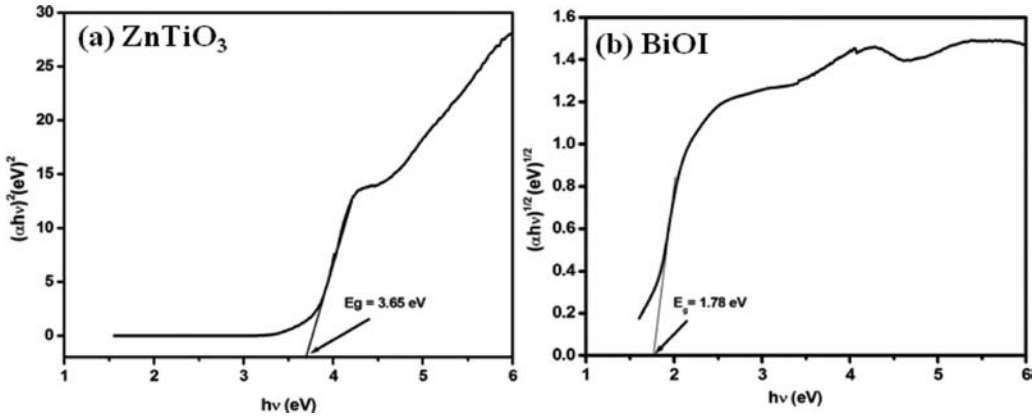

Figure 10. (a) Plots of $(\alpha h\nu)^2$ vs photon energy $(h\nu)$ for the band gap energy of $ZnTiO_3$ and (b) plots of $(\alpha h\nu)^{1/2}$ vs photon energy $(h\nu)$ for the band gap energy of BiOI.

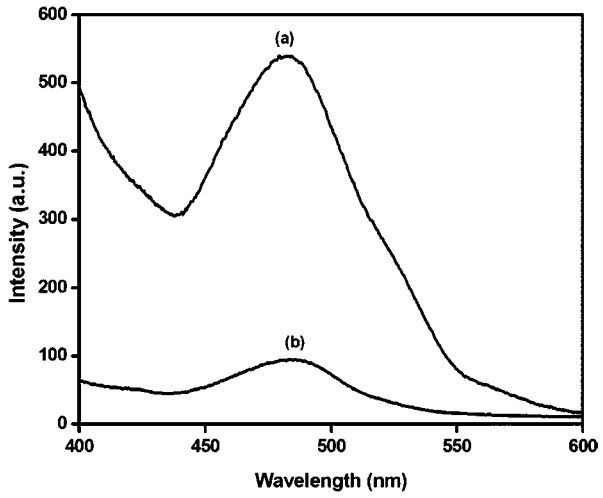

Figure 11. Photoluminescence emission spectra of (a) $ZnTiO_3$ and (b) 50% $BiOI/ZnTiO_3$ heterojunction measured at room temperature with 350 nm wavelength excitation.

observed that $ZnTiO_3$ generates an anodic photocurrent with applied bias. The generation of anodic photocurrent shows that $ZnTiO_3$ is a n-type semiconductor. The flat band potential of $ZnTiO_3$ is observed at −0.94 V versus Ag/AgCl at pH 6. The flat band potential is strongly related to the bottom of the conduction band and is considered to be the conduction band minimum for n-type $ZnTiO_3$.[50] Since the band gap energy of $ZnTiO_3$ is 3.65 eV, the valence band maximum was estimated to be 2.71 eV. The BiOI was able to generate cathodic photocurrent with applied bias. The cathodic photocurrent suggests the p-type character of BiOI. The photocurrent onset potential of BiOI gives the value of the valence band edge. The photocurrent onset potential of BiOI was observed at +0.79 V versus Ag/AgCl at pH 6. So, the valence band edge of BiOI was lying at +0.79 V.[45,51] The band gap energy of BiOI is 1.78 eV. Therefore, the conduction band minimum was estimated to be −0.99 V. The calculated band edge positions of p-type BiOI and n-type $ZnTiO_3$ are represented in Scheme 1.

Photocatalytic Activity. The semiconducting materials absorb photons with energy greater than that of the band gap energy, excite electrons from valence band to conduction band, and leave holes in the valence band. The photogenerated electron−hole pairs in the bulk materials are separated and then move to the photocatalyst surface without recombination. The electron−hole pairs present on the surface of the material react with the surface adsorbed species and produce degradation products. The photocatalytic activities of the pure $ZnTiO_3$, BiOI, and $BiOI/ZnTiO_3$ heterojunctions were evaluated by degradation of Rh 6G solutions under visible light irradiation. The photocatalytic reactions of the prepared samples were performed under three different conditions: (i) Degradation of the Rh 6G was monitored under visible light for 3 h without using photocatalysts. From this experiment, it was observed

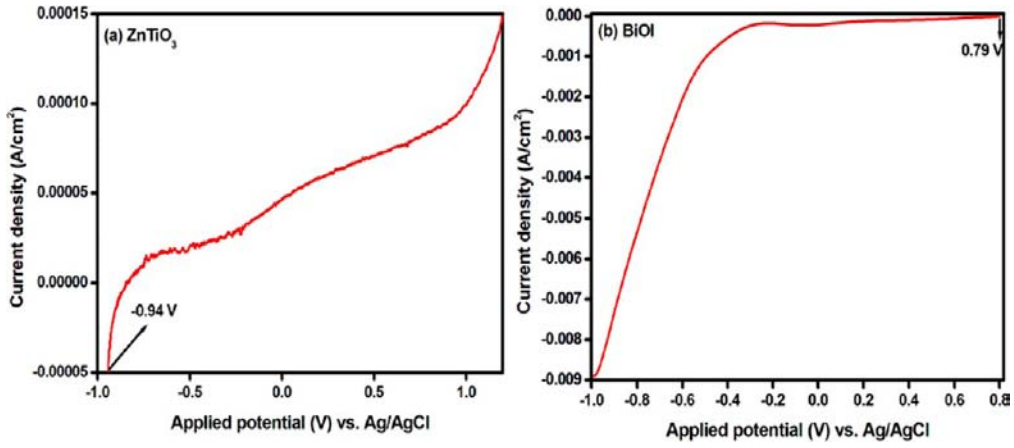

Figure 12. Current−potential curves for (a) $ZnTiO_3$ and (b) BiOI under Xe light irradiation ($\lambda \geq 300$ nm).

dx.doi.org/10.1021/ic400159m | Inorg. Chem. 2013, 52, 6390−6401

Scheme 1. Band Edge Positions of n-Type $ZnTiO_3$ and p-Type BiOI Calculated at pH 6 versus Ag/AgCl

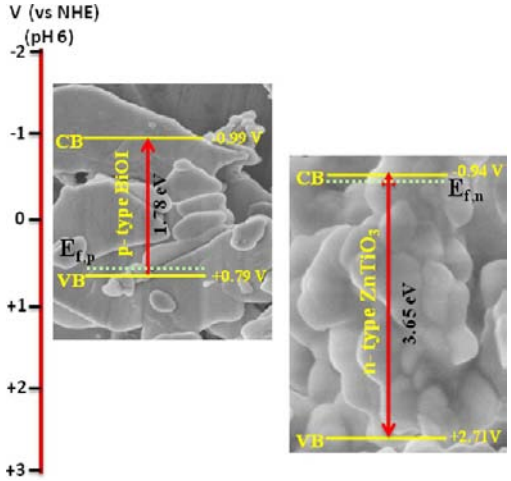

that the concentration of Rh 6G hardly decomposed under visible light irradiation in the absence of the photocatalyst. (ii) The control experiments were performed for 1 h under the dark condition in presence of photocatalysts, which indicated the adsorption of dyes on the active sites of the photocatalyst. (iii) Lastly, the degradation of Rh 6G was monitored in presence of all the photocatalysts and visible light. The percentage of Rh 6G degradation over all the photocatalysts as a function of the exposure time is represented in Figure13.

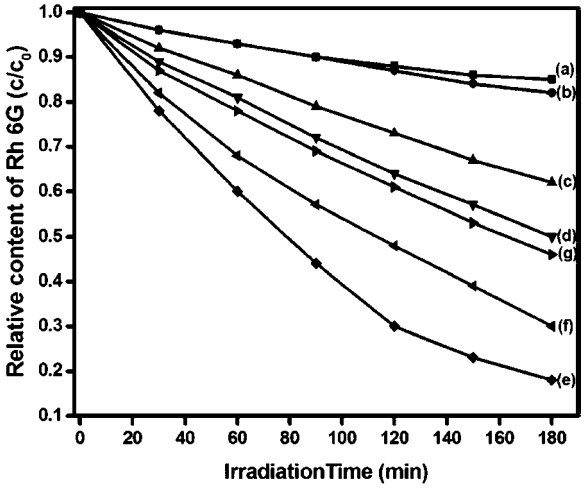

Figure 13. Photocatalytic degradation of Rh 6G over (a) $ZnTiO_3$, (b) BiOI, (c) 10 mol % BiOI/$ZnTiO_3$, (d) 30 mol % BiOI/$ZnTiO_3$, (e) 50 mol % BiOI/$ZnTiO_3$, (f) 70 mol % BiOI/$ZnTiO_3$, (g) 90 mol % BiOI/$ZnTiO_3$.

The percentage of degradation of Rh 6G over all the photocatalysts follows the following order: 50% BiOI/$ZnTiO_3$ > 70% BiOI/$ZnTiO_3$ > 90% BiOI/$ZnTiO_3$ > 30% BiOI/$ZnTiO_3$ > 10%BiOI/$ZnTiO_3$ > BiOI > $ZnTiO_3$. Moreover, the percentage of degradation increases with the increase of BiOI concentration in the BiOI/$ZnTiO_3$ heterojunctions up to 50% and then decreases with further increasing BiOI concentration. Therefore, the critical molar proportion of BiOI to $ZnTiO_3$ was found to be 50% which exhibits the best photocatalytic activity toward degradation of Rh 6G over all the photocatalysts. The said photocatalyst was able to degrade 82% of Rh 6G solution in 3 h under visible light irradiation. The kinetics of Rh 6G degradation under visible light over all the photocatalysts was investigated by applying the Langmuir–Hinshelwood model.[52]

$$\ln(C_0/C) = kt$$

Here, k is the pseudo-first-order rate constant. The plots $\ln(C_0/C)$ versus irradiation time (where C_0 is the initial concentration of the dye and C is the concentration of the dye in the reaction time) were found to be linear as shown in Figure 14, and this

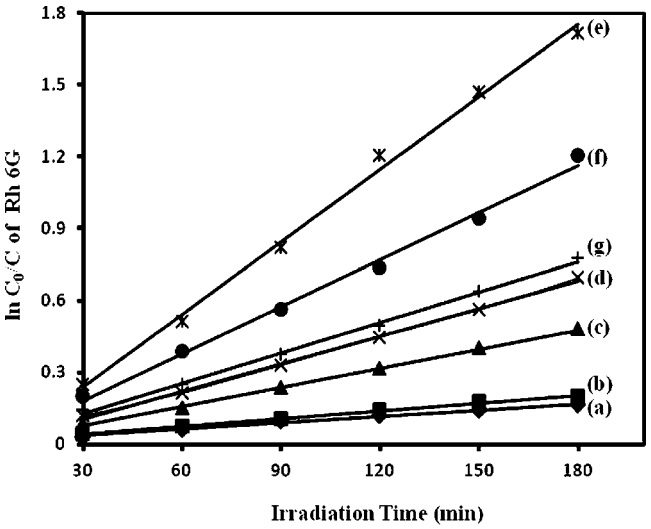

Figure 14. Pseudo-first-order kinetics of (a) $ZnTiO_3$, (b) BiOI, (c) 10 mol % BiOI/$ZnTiO_3$, (d) 30 mol % BiOI/$ZnTiO_3$, (e) 50 mol % BiOI/$ZnTiO_3$, (f) 70 mol % BiOI/$ZnTiO_3$, (g) 90 mol % BiOI/$ZnTiO_3$.

suggests that photodegradation reactions follow pseudo-first-order kinetics. The apparent reaction rate constants (k) for the photocatalytic degradation of Rh 6G were evaluated from experimental data using a linear regression. In all cases, the R^2 (correlation coefficient) value was greater than 0.99, which confirmed the proposed rate law for Rh 6G degradation. The apparent rate constants for $ZnTiO_3$, BiOI, 10% BiOI/$ZnTiO_3$, 30% BiOI/$ZnTiO_3$, 50% BiOI/$ZnTiO_3$, 70% BiOI/$ZnTiO_3$, and 90% BiOI/$ZnTiO_3$ were determined as 0.0009, 0.0011, 0.0027, 0.0039, 0.0101, 0.0065, and 0.0043 min^{-1}, respectively. The decreasing order of rate constants is summarized as follows: 50% BiOI/$ZnTiO_3$ > 70% BiOI/$ZnTiO_3$ > 90% BiOI/$ZnTiO_3$ > 30% BiOI/$ZnTiO_3$ > 10%BiOI/$ZnTiO_3$ > BiOI > $ZnTiO_3$, which is consistent with the photocatalytic degradation results presented in Figure 13. The corresponding k values of BiOI/$ZnTiO_3$ heterojunctions were much higher than that of BiOI and $ZnTiO_3$. Especially, 50% BiOI/$ZnTiO_3$ exhibited the highest k value (0.0101 min^{-1}) which was about 9.8 times higher than that of BiOI and 11.1 times higher than that of $ZnTiO_3$ indicating that it had the best photocatalytic activity for decomposing Rh 6G under visible light irradiation. From the above degradation results, we conclude that all the BiOI/$ZnTiO_3$ heterojunctions exhibit much higher photocatalytic activities than that of single phase BiOI and $ZnTiO_3$. The enhancement of the photocatalytic activities of the BiOI/$ZnTiO_3$ heterojunctions in comparison to individual components may be due to the following two reasons: (i) BiOI is capable to extend the absorption of $ZnTiO_3$ in the visible region due to its sensitization character. (ii) The p–n junction

dx.doi.org/10.1021/ic400159m | Inorg. Chem. 2013, 52, 6390–6401

formed between the p-type BiOI and n-type $ZnTiO_3$ helps in separating electron−hole pairs at the interface. The detailed mechanism of the separation of the electron−hole pairs at the p−n junction interface is schematically represented in Figure15.

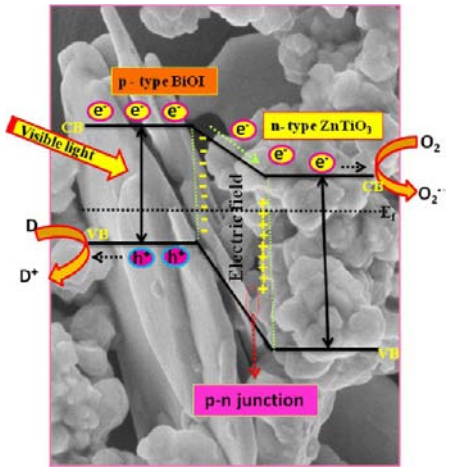

Figure 15. Proposed charge separation and degradation process of p-type BiOI/n-type $ZnTiO_3$ heterojunctions under visible light irradiation ($\lambda \geq 400$ nm).

From the PEC measurement, we found that BiOI is a p-type semiconductor whereas $ZnTiO_3$ is a n-type semiconductor. For p-type BiOI the Fermi level lies above the valence band whereas the Fermi level lies below the conduction band for n-type $ZnTiO_3$ as shown in Scheme 1. When p-type BiOI combines with n-type $ZnTiO_3$, a p−n junction is formed between them, and the charge carriers diffuse in opposite direction to form an internal electric field at the heterojunction interface. Under thermal equilibrium conditions, the Fermi levels of n-$ZnTiO_3$ and p-BiOI are aligned, and an internal electric field directed from n-$ZnTiO_3$ to p-BiOI is simultaneously built to stop the charge diffusion from n-$ZnTiO_3$ into p-BiOI. Meanwhile, the energy band positions of $ZnTiO_3$ are shifted toward the downward direction and that of BiOI toward the upward direction along with the Fermi level.[26,27] Therefore, the band positions of the p-type BiOI and n-type $ZnTiO_3$ in the heterojunction have a type-II band structure. According to type-II band structure, the CB and VB of BiOI lie above the CB and VB of $ZnTiO_3$. Under visible-light irradiation, BiOI absorbs photons of energy greater than the band gap energy, which excite the electrons in the VB to the CB and leave holes in the VB of BiOI. The electrons in the conduction band of the p-type BiOI are then transferred to the n-type $ZnTiO_3$, and the holes remain in the valence band of BiOI. The migration of photogenerated carriers can be promoted by the inner electric field established at the heterojunction interfaces. Thus, the photogenerated electron−hole pairs will be effectively separated due to the formation of a junction between the p-BiOI and n-$ZnTiO_3$ interface, resulting in a reduced electron−hole recombination.[26]

The separated electrons and holes are then free to initiate the degradation reaction of Rh 6G dye adsorbed on the photocatalyst surfaces with enhanced photocatalytic activity. The potential photocatalytic process in the degradation of Rh 6G may involve several steps: (i) The CB electrons (e^-) accumulated on the surface of $ZnTiO_3$ are then scavenged by oxygen on the surface of the catalyst to form super oxide radicals ($O_2^{\bullet -}$), which again react with protons and photogenerated electrons to provide hydroxyl radical species ($OH^\bullet$). (ii) Holes in the BiOI may directly oxidize the organic molecules. The formations of these highly active species, i.e., superoxide radicals, hydroxyl radicals, or holes, are mostly responsible for degradation of organic pollutants.[53] The details are presented below:

$$BiOI/ZnTiO_3 + h\nu \rightarrow ZnTiO_3(e^-) + BiOI(h^+)$$

$$ZnTiO_3(e^-) + O_2 \rightarrow O_2^{\bullet -}$$

$$O_2^{\bullet -} + H^+ \rightarrow HO_2^\bullet$$

$$HO_2^\bullet + H^+ + ZnTiO_3(e^-) \rightarrow H_2O_2$$

$$H_2O_2 + ZnTiO_3(e^-) \rightarrow OH^\bullet + OH^-$$

$$Rh6G + OH^\bullet \rightarrow \text{degradation products}$$

$$Rh6G + BiOI(h^+) \rightarrow \text{degradation products}$$

The regeneration, reuse, and stability of the photocatalyst are the three major factors of a catalyst to be used in the practical applications. The highest result yielding catalyst was regenerated by centrifugation after degradation reaction and washed with water 4−5 times for the complete removal of dye from the catalysts. Then the catalyst was dried at 80 °C for 12 h and reused for another cycle keeping the concentration of dye and photocatalyst unchanged. The photocatalytic activity was found to be nearly the same up to four cycles which determined the stability of the photocatalysts as shown in Figure 16.

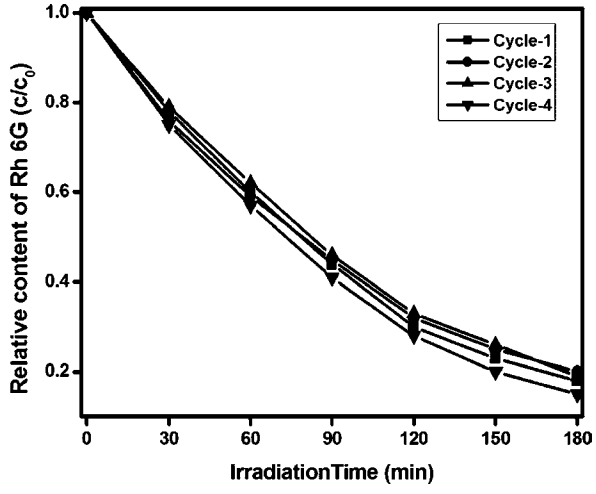

Figure 16. Regeneration, reuse, and stability test over 50% BiOI/$ZnTiO_3$ heterojunction.

The formation of $OH^\bullet$ radicals in all the photocatalysts under visible light irradiation was detected by fluorescence technique using terephthalic acid (TA) as a probe agent. The $OH^\bullet$ radical is known to be readily trapped by TA to produce the fluorescent 2-hydroxyterephthalic acid, and its fluorescence intensity is directly proportional to the amount of $OH^\bullet$ radicals formed in the water. The greater the formation of $OH^\bullet$ radicals, the higher the separation rate of electron−hole pairs in the photocatalysts.[54]

$$OH^- + TA \rightarrow TAOH$$

dx.doi.org/10.1021/ic400159m | Inorg. Chem. 2013, 52, 6390−6401

The fluorescence intensity signals were measured after 180 min irradiation, and the formation of hydroxyl radicals over all $BiOI/ZnTiO_3$ heterojunctions followed the following order: 50% $BiOI/ZnTiO_3$ > 70% $BiOI/ZnTiO_3$ > 90% $BiOI/ZnTiO_3$ > 30% $BiOI/ZnTiO_3$ > 10% $BiOI/ZnTiO_3$, which agrees well with the photocatalytic activity results shown in Figure 17.

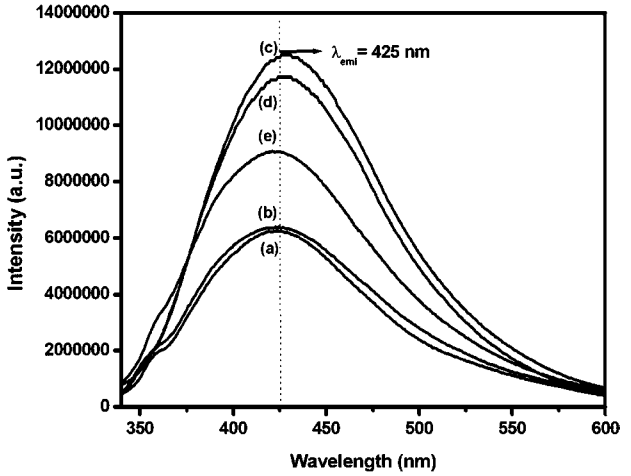

Figure 17. Fluorescence spectra of (a) 10 mol % $BiOI/ZnTiO_3$, (b) 30 mol % $BiOI/ZnTiO_3$, (c) 50 mol % $BiOI/ZnTiO_3$, (d) 70 mol % $BiOI/ZnTiO_3$, (e) 90 mol % $BiOI/ZnTiO_3$ in a 5×10^{-5} M basic solution of terephthalic acid.

4. CONCLUSIONS

The $BiOI/ZnTiO_3$ heterojunctions were successfully synthesized by a precipitation−deposition method. The formation of $BiOI/ZnTiO_3$ heterojunctions was confirmed by PXRD. The narrow band gap of BiOI effectively sensitized the wide band gap of $ZnTiO_3$ in the visible region, confirmed by UV−vis DRS. The surface morphology, the interaction, and formation of the interface between BiOI and $ZnTiO_3$ in the $BiOI/ZnTiO_3$ heterojunction were well explained by FESEM, TEM, and HRTEM. The p−n junction effect and the PL study showed the efficient separation of the photogenerated charge carriers which leads to enhanced photocatalytic activities. Among all the heterojunctions, the 50% $BiOI/ZnTiO_3$ exhibits the highest result, i.e., 82% of Rh 6G degradation under visible light irradiation. The degradation rate of 50% $BiOI/ZnTiO_3$ heterojunctions was found to be 9.8 and 11.1 times higher than that of bare BiOI and $ZnTiO_3$.

AUTHOR INFORMATION

Corresponding Author

*E-mail: paridakulamani@yahoo.com. Phone: +91-674-2379425. Fax: +91-674-2581637.

Notes

The authors declare no competing financial interest.

ACKNOWLEDGMENTS

The authors are very thankful to Prof. B.K. Mishra, Director, IMMT, Bhubaneswar, for giving permission to publish the work. The financial assistance by CSIR in the form of CSIR-TAPSUN programme is greatly acknowledged. Mr. B. N. Biswal is greatly acknowledged for helping us to take PL spectra. The authors K.H.R. and S.M. are thankful to CSIR, New Delhi, for SRF. Prof. A. C. Dash is greatly acknowledged for English correction of the manuscript.

REFERENCES

(1) Zhou, X.; Liu, G.; Yu, J.; Fan, W. *J. Mater. Chem.* **2012**, *22*, 21337−21354.
(2) Kudo, A.; Miseki, Y. *Chem. Soc. Rev.* **2009**, *38*, 253−278.
(3) Albu, S. P.; Ghicov, A.; Macak, J. M.; Hahn, R.; Schmuki, P. *Nano Lett.* **2007**, *7*, 1286−1289.
(4) Kato, H.; Asakura, K.; Kudo, A. *J. Am. Chem. Soc.* **2003**, *125*, 3082−3089.
(5) Ishihara, T.; Nishiguchi, H.; Fukamachi, K.; Takkkita, Y. *J. Phys. Chem. B* **1999**, *103*, 1−3.
(6) Domen, K.; Naito, S.; Soma, S.; Onishi, M.; Tamaru, K. *J. Chem. Soc., Chem. Commun.* **1980**, 543−544.
(7) Wang, W. P.; Yang, H.; Xian, T.; Li, R. S.; Ma, J. Y.; Jiang, J. L. *Adv. Sci., Eng. Med.* **2012**, *4*, 479−483.
(8) Arney, D.; Watkins, T.; Maggard, P. A. *J. Am. Ceram. Soc.* **2011**, *94*, 1483−1489.
(9) Konga, J. Z.; Li, A. D.; Zhai, H. F.; Li, H.; Yan, Q. Y.; Ma, J.; Wu, D. *J. Hazard. Mater.* **2009**, *171*, 918−923.
(10) Kim, H. T.; Byun, J. D.; Kim, Y. *Mater. Res. Bull.* **1998**, *33*, 963−973.
(11) Obayashi, H.; Sakurai, Y.; Gejo, T. *J. Solid State Chem.* **1976**, *17*, 299−303.
(12) Kim, H. T.; Nahm, S.; Byun, J. D. *J. Am. Ceram. Soc.* **1999**, *82*, 3043−3048.
(13) Liu, X. C.; Gao, F.; Zhao, L. L.; Tian, C. S. *J. Alloys Compd.* **2007**, *436*, 285−289.
(14) Ye, C.; Wang, Y.; Ye, Y.; Zhang, J.; Li, G. H. *J. Appl. Phys.* **2009**, *106*, 033520(1−4).
(15) Stoyanova, A.; Hitkova, H.; Bachvarova-nedelcheva, A.; Iordanova, R.; Ivanova, N.; Sredkova, M. *Dig. J. Nanomater. Biostruct.* **2012**, *7*, 777−784.
(16) Bai, J.; Li, J.; Liu, Y.; Zhou, B.; Cai, W. *Appl. Catal., B* **2010**, *95*, 408−413.
(17) Xie, Y.; Ali, G.; Yoo, S. H.; Cho, S. O. *ACS Appl. Mater. Interfaces* **2010**, *2*, 2910−2914.
(18) Zhang, X.; Zhang, L.; Xie, T.; Wang, D. *J. Phys. Chem. C* **2009**, *113*, 7371−7378.
(19) Li, X.; Huang, R.; Hu, Y.; Chen, Y.; Liu, W.; Yuan, R.; Li, Z. *Inorg. Chem.* **2012**, *51*, 6245−6250.
(20) Gui, M. S.; Zhang, W. D. *Nanotechnology* **2011**, *22*, 265601.
(21) Wang, K.; Jia, F.; Zhang, L. *Mater. Lett.* **2013**, *92*, 354−357.
(22) Kong, L.; Jiang, Z.; Xiao, T.; Lu, L.; Jones, M. O.; Edwards, P. P. *Chem. Commun.* **2011**, *47*, 5512−5514.
(23) Xiao, X.; Zhang, W. D. *J. Mater. Chem.* **2010**, *20*, 5866−5870.
(24) Li, Y.; Wang, J.; Liu, B.; Dang, L.; Yao, H.; Li, Z. *Chem. Phys. Lett.* **2011**, *508*, 102−106.
(25) Dai, G.; Yu, J.; Liu, G. *J. Phys. Chem. C* **2011**, *115*, 7339−7346.
(26) Cao, J.; Xu, B.; Lin, H.; Luo, B.; Chen, S. *Dalton Trans.* **2012**, *41*, 11482−11490.
(27) Jiang, J.; Zhang, X.; Sun, P.; Zhang, L. *J. Phys. Chem. C* **2011**, *115*, 20555−20564.
(28) Cheng, H.; Huang, B.; Dai, Y.; Qin, X.; Zhang, X. *Langmuir* **2010**, *26*, 6618−6624.
(29) Li, Y.; Wang, J.; Yao, H.; Dang, L.; Li, Z. *Catal. Commun.* **2011**, *12*, 660−664.
(30) Yu, C.; Yu, J. C.; Fan, C.; Wen, H.; Hu, S. *Mater. Sci. Eng., B* **2010**, *166*, 213−219.
(31) Li, T. B.; Chen, G.; Zhou, C.; Shen, Z. Y.; Jin, R. C.; Sun, J. X. *Dalton Trans.* **2011**, *40*, 6751−6758.
(32) Chen, L.; Yin, S. F.; Luo, S. L.; Huang, R.; Zhang, Q.; Hong, T.; Au, P. C. T. *Ind. Eng. Chem. Res.* **2012**, *51*, 6760−6768.
(33) Zhu, L.; He, C.; Huang, Y.; Chen, Z.; Xia, D.; Su, M.; Xiong, Y.; Li, S.; Shu, D. *Sep. Purif. Technol.* **2012**, *91*, 59−66.
(34) Chaouchi, A.; Saidi, M.; Astorg, S.; Marinel, S. *Process. Appl. Ceram.* **2012**, *6*, 83−89.

(35) Wang, S. F.; Gu, F.; Lu, M. K.; Song, C. F.; Liu, S. W.; Xu, D.; Yuan, D. R. *Mater. Res. Bull.* **2003**, *38*, 1283−1288.
(36) Mohapatra, L.; Parida, K. M.; Satpathy, M. *J. Phys. Chem. C* **2012**, *116*, 13063−13070.
(37) Roussel, H.; Briois, V.; Elkaim, E.; Roy, A.; Besse, J. P. *J. Phys. Chem. B* **2000**, *104*, 5915−5923.
(38) Zhanga, H.; Wua, X.; Wang, Y.; Chen, X.; Li, Z.; Yu, T.; Ye, J.; Zou, Z. *J. Phys. Chem. Solids* **2007**, *68*, 280−283.
(39) Hassanzadeh, A.; Moazzez, B.; Haghgooie, H.; Nasseri, M.; Golzan, M. M.; Sedghi, H. *Cent. Eur. J. Chem.* **2008**, *6*, 651−656.
(40) Lin, X.; Huang, F.; Xing, J.; Wang, W.; Xu, F. *Acta Mater.* **2008**, *56*, 2699−2705.
(41) Krylova, G.; Brioude, A.; Ababou-Girard, S.; Mrazeka, J.; Spanhel, L. *Phys. Chem. Chem. Phys.* **2010**, *12*, 15101−15110.
(42) Zhang, Z.; Shao, C.; Li, X.; Wang, C.; Zhang, M.; Liu, Y. *ACS Appl. Mater. Interfaces* **2010**, *2*, 2915−2923.
(43) *Handbook of X-ray Photoelectron Spectroscopy*; Wagner, C. D., Riggs, W. M., Davis, L. E., Moulder, J. F., Muilenberg, G. E., Eds.; Perkin-Elmer Co.: Waltham, MA, 1979.
(44) Ye, L.; Tian, L.; Peng, T.; Zan, L. *J. Mater. Chem.* **2011**, *21*, 12479−12484.
(45) Reddy, K. H.; Martha, S.; Parida, K. M. *RSC Adv.* **2012**, *2*, 9423−2436.
(46) Bian, Z.; Zhu, J.; Wang, S.; Cao, Y.; Qian, X.; Li, H. *J. Phys. Chem. C* **2008**, *112*, 6258−6262.
(47) Tang, J. W.; Zou, Z. G.; Ye, J. H. *J. Phys. Chem. B* **2003**, *107*, 14265−69.
(48) Xu, Q. C.; Wellia, D. V.; Ng, Y. H.; Amal, R.; Tan, T. T. Y. *J. Phys. Chem. C* **2011**, *115*, 7419−7428.
(49) Li, Z. X.; Shi, F. B.; Ding, Y.; Zhang, T.; Yan, C. H. *Langmuir* **2011**, *27*, 14589−14593.
(50) Wang, Z.; Hou, J.; Jiao, S.; Huang, K.; Zhu, H. *J. Mater. Chem.* **2012**, *22*, 21972−12978.
(51) Parida, K. M.; Nashim, A.; Mahanta, S. K. *Dalton Trans.* **2011**, *40*, 12839−12845.
(52) Hou, J.; Wang, Z.; Jiao, S.; Zhu, H. *CrystEngComm* **2012**, *14*, 5923−5928.
(53) Zheng, L.; Zheng, Y.; Chen, C.; Zhan, Y.; Lin, X.; Zheng, Q.; Wei, K.; Zhu, J. *Inorg. Chem* **2009**, *48*, 1819−1825.
(54) Parida, K. M.; Mohapatra, L.; Baliarsingh, N. *J. Phys. Chem. C* **2012**, *116*, 22417−22424.

dx.doi.org/10.1021/ic400159m | *Inorg. Chem.* 2013, 52, 6390−6401